nature geoscience

Article

https://doi.org/10.1038/s41561-022-01112-z

Multidecadal variation of the Earth's inner-core rotation

Received: 21 December 2021

Accepted: 5 December 2022

Published online: 23 January 2023

Check for updates

Yi Yang & Xiaodong Song

Differential rotation of Earth's inner core relative to the mantle is thought to occur under the effects of the geodynamo on core dynamics and gravitational core–mantle coupling. This rotation has been inferred from temporal changes between repeated seismic waves that should traverse the same path through the inner core. Here we analyse repeated seismic waves from the early 1990s and show that all of the paths that previously showed significant temporal changes have exhibited little change over the past decade. This globally consistent pattern suggests that inner-core rotation has recently paused. We compared this recent pattern to the Alaskan seismic records of South Sandwich Islands doublets going back to 1964 and it seems to be associated with a gradual turning-back of the inner core as a part of an approximately seven-decade oscillation, with another turning point in the early 1970s. This multidecadal periodicity coincides with changes in several other geophysical observations, especially the length of day and magnetic field. These observations provide evidence for dynamic interactions between the Earth's layers, from the deepest interior to the surface, potentially due to gravitational coupling and the exchange of angular momentum from the core and mantle to the surface.

Earth's inner core gradually grows from the cooling and solidification of a liquid outer core to the present radius of ~1,220 km. The chemical buoyancy and latent heat released from the iron phase transition at the inner-core boundary (ICB) power the outer-core convection and the geodynamo that generate the Earth's magnetic field[1]. The electromagnetic (EM) torque from the geodynamo tends to rotate the inner core in the liquid outer core[2–4]. Seismic observations suggest a highly heterogeneous inner core, with fine-scale scatters[5], regional velocity variations[6–8] and long-wavelength to hemispherical structures[9–11]. It is also believed that the gravitational coupling between the heterogeneous mantle and inner core slows down the relative rotation or turns it into an oscillation[12–16].

Evidence for the differential rotation of the Earth's inner core was first reported from temporal changes of the seismic waves traversing it (PKIKP, commonly referred as DF; Fig. 1) over years or decades from the South Sandwich Islands (SSI) to the College seismic station (code COL; Fig. 1) in Alaska[17]. The inner-core temporal changes were subsequently confirmed, particularly from collocated nuclear blasts[18] or earthquake waveform doublets[19,20], which are repeating earthquakes with nearly identical waveforms at common receivers[21]. The temporal changes have also been interpreted as localized growth or melting at the ICB, without the necessity of invoking the inner-core differential rotation[22–24]. However, more recent studies[25–27] suggest that the temporal changes are related to the interior rather than surficial heterogeneities of the inner core, still favouring the interpretation of the differential rotation. Using high-quality global doublets and lower-quality SSI doublets, here, we show surprising observations that indicate the inner core has nearly ceased its rotation in the recent decade and may be experiencing a turning-back in a multidecadal oscillation, with another turning point in the early 1970s.

Global observations of the inner-core temporal changes

We systematically investigated the temporal changes of inner-core PKP waves (Fig. 1) along all known paths from previous studies of earthquake

SinoProbe Laboratory and Institute of Theoretical and Applied Geophysics, School of Earth and Space Sciences, Peking University, Beijing, China.
e-mail: xiao.d.song@gmail.com

https://doi.org/10.1038/s41561-022-01112-z

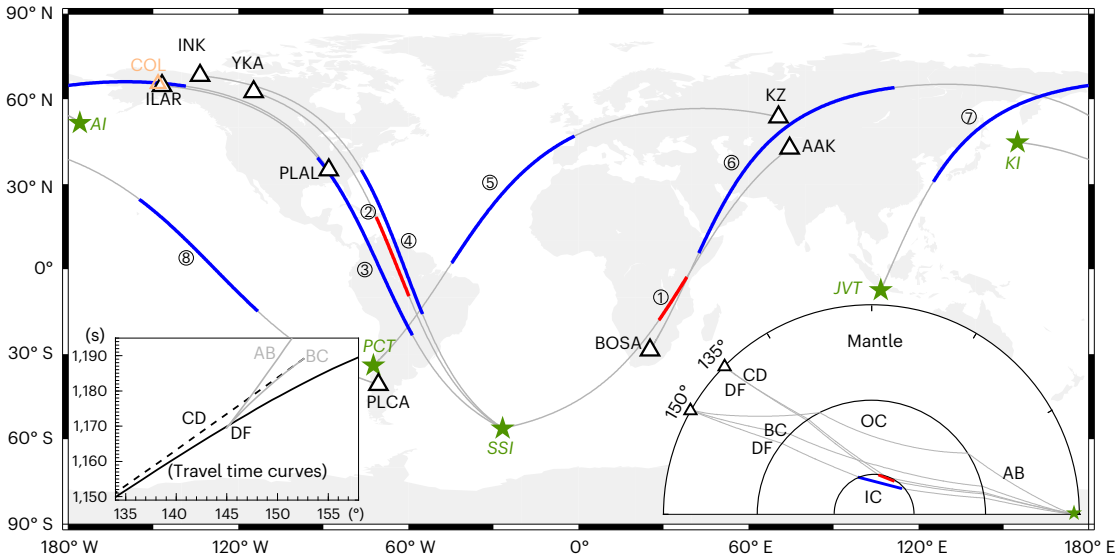

Fig. 1 | Seismic raypaths used in the study. There are eight different paths from repeating earthquakes (stars) to seismic stations or arrays (triangles), including: (1) SSI to station AAK; (2) SSI to Yellowknife array (YKA); (3) SSI to ILAR array; (4) SSI to station INK; (5) Peru–Chile trench (PCT) to Kazakhstan network (KZ); (6) Aleutian Islands (AI) to station BOSA; (7) Java trench (JVT) to station PLAL; and (8) Kurile Islands (KI) to station PLCA. The thickened lines indicate the ray segments in the inner core (IC); their colours, red and blue, denote the DF rays from the CD and BC distance ranges, respectively. The two insets show the travel time curves and raypaths of different PKP branches, including the DF branch traversing the IC, the BC and AB branches traversing the outer core (OC) and the CD branch reflecting at the ICB.

doublets[19,20,22,28–31]. We divided the paths into two groups according to their epicentral distances. One is at the larger (BC) distance range (for example, 150°; Fig. 1), where the outer-core BC arrival is observable several seconds after the inner-core DF arrival. The other is at the smaller (CD) distance range (for example, 135°; Fig. 1), where the DF arrival is closely followed by the CD (PKiKP) arrival reflecting off the ICB. Figure 1 shows a collection of paths with previously discovered inner-core temporal changes and updated doublets of extremely high quality from our systematic search (Methods, Supplementary Information and Supplementary Tables 1 and 2).

We quantified the temporal changes in terms of waveform similarity (S) for all the paths and double differential time (ddt, difference in the differential time between BC and DF phases from the two events of the doublet) for the paths at the BC range (see Methods for details). The S is measured with waveform cross-correlation but corrected for the influence of background noises ($S = 1$ representing a perfect match if noise-free). A significantly small S (below the reference value of 0.95 based on the mantle and outer-core seismic phases) and a significantly non-zero ddt imply significant temporal changes in the waveforms and arrival times of the inner-core waves, respectively. The main uncertainties of the S and ddt measurements (σ_s and σ_t, respectively) come from the background noises, as the inner-core phases are relatively weak.

Observations of a pause of rotation in the recent decade

Surprisingly, the significant temporal changes along all the paths stop appearing in the recent decade or so from observations of both S and ddt. We discuss the change in S first. Figure 2a,b displays representative examples, which compare the waveforms from one multiplet (a sequence of repeating earthquakes) in the SSI region to two different receivers at the CD and BC ranges, respectively. The multiplet is of great quality as indicated by the highly similar outer-core BC arrivals shown in Fig. 2b and all available non-inner-core arrivals at other stations (Supplementary Information). At both distance ranges, there are obvious misalignments of the inner-core waveforms from the earlier two repeaters (in 1998 and 2004) with S below 0.6, while the waveforms between the two recent repeaters of the same multiplet (in 2009 and 2017, over an even longer duration) are highly similar with S of ~1.0. We found at least one multiplet with such a pattern for each known path with temporal changes of PKP waves (Extended Data Fig. 1). Pairs in the earlier periods always have smaller S values (ranging from 0.29 to 0.88) than the recent pairs in the same multiplet (0.95 or greater). The consistency within either time period and the contrast between the two periods are remarkable (Fig. 2 and Extended Data Figs. 1 and 2), pointing to a systematic change over the two time periods.

In addition to the powerful comparison of the multiplets, we systematically examined all the doublets and obtained 172 S measurements from both distance ranges (Extended Data Fig. 3 and Supplementary Table 3). The result is the same as exemplified by the multiplets. To better compare the temporal changes across different periods, we used two subsets of the S measurements, one with 23 measurements from the doublets whose events are both before 2009, and the other with 43 measurements from the doublets whose events are both after 2009 (Fig. 3). The contrast between the two subsets is striking. For the older subset, the S values are all below the reference of 0.95, except for a few doublets with a small lapse of less than 3.5 years, which is too short to accumulate observable temporal changes[19,20,30]. For the second subset, the S measurements are all scattered around the reference.

We also observed a clear pattern change in the ddt measurements in the recent decade. We obtained 64 ddt measurements during 1995–2020 from the six paths at the BC range and found significantly non-zero (over two σ_t) ddt measurements along all of them, indicating the existence of the lateral velocity gradients under the model of inner-core rotation[6]. Assuming the same small patch of the inner core (mostly less than 60 km; Supplementary Table 4) sampled by each path has a constant lateral velocity gradient, it is straightforward to track the pattern of the rotation from the ddt measurements. However, the velocity gradients sampled by different paths may vary greatly. In fact, most parts of the inner core show indiscernible lateral gradients, too small to produce observable temporal changes from doublets over years or decades[20].

We used a cubic spline to approximate the accumulated amount of differential rotation over time, which is linearly proportional to the temporal variation of the DF's travel time relative to the BC phase (dt)

https://doi.org/10.1038/s41561-022-01112-z

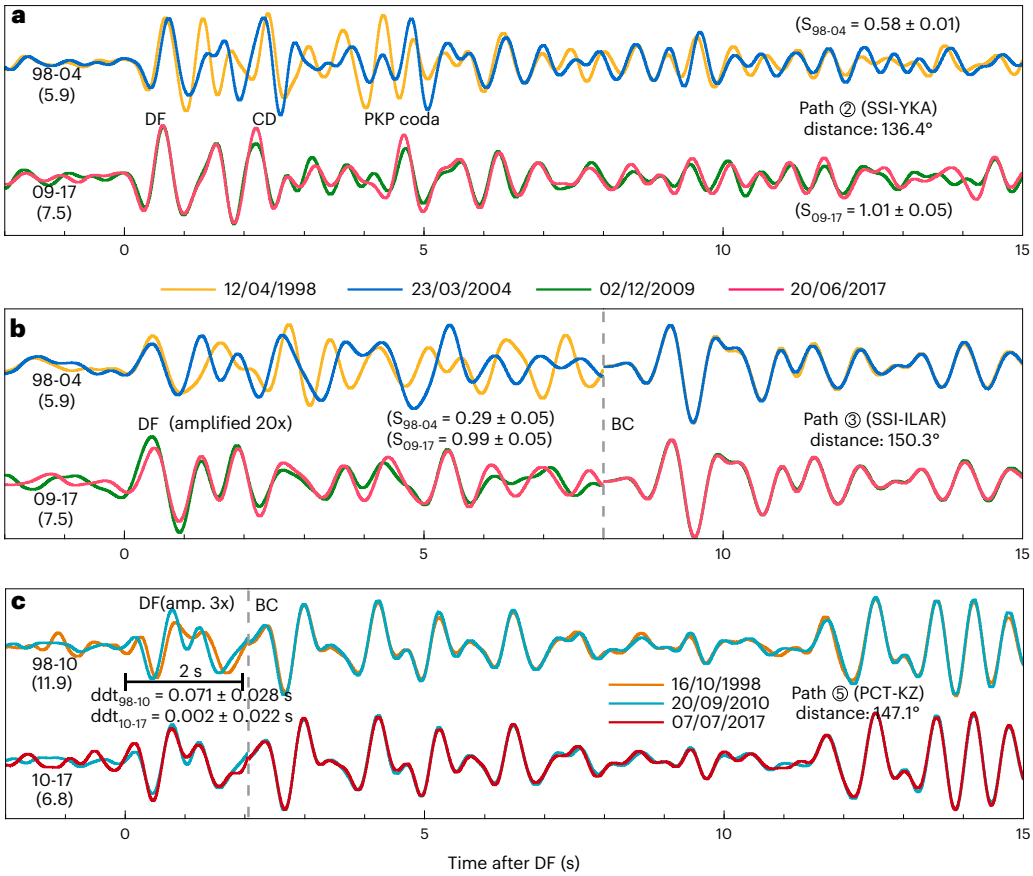

Fig. 2 | Examples highlighting a pattern change in the inner-core temporal changes in the recent decade. a,**b**, Waveforms from an SSI multiplet along Paths 2 and 3 showing the pattern change in *S*. The last two digits of the event years and time lapse (in years) are labelled on the left. For Path 2 at CD distance range (**a**), the normalized waveforms are aligned by cross-correlation of the entire window. For Path 3 at BC distance range (**b**), they are aligned with BC, and the weak inner-core waves and the background noise preceding the dashed line (onset of BC) are amplified. **c**, Waveforms from a PCT multiplet along Path 5 showing the pattern change in DF relative arrival times (ddt). It is plotted in the same way as **b**. The horizontal 2-s segment is the DF time window used to measure the ddt.

scaled by a path-dependent factor. The spline remains the same for all the paths but the scaling factor represents the lateral gradient of the corresponding path relative to the reference path (Path 5 in Fig. 1), which has the most ddt observations. We jointly inverted the spline coefficients and the path-dependent factors with all the ddt measurements and obtained the model uncertainty with the bootstrap method[32] (Methods). The best-fitting spline shows a clear increasing trend from 1995 to 2009 but a flattening or slightly decreasing trend since then (Fig. 4a and Extended Data Fig. 4).

A closer examination suggests a slight decrease in the dt curve after 2009 or so. The best-fitting spline depicts a gradual deceleration over a few years before the overturn (time of zero gradient) in late 2009. From the bootstrapping, the 95% confidence interval (CI) for the time of the overturn is (2009.0, 2011.0) and the negative trend since 2009 is highly robust, at $-1.58\pm^{1.21}_{1.11}$ ms yr^{-1} (95% confidence), in contrast to the trend before 2009, at $9.12\pm^{0.72}_{0.52}$ ms yr^{-1}. The similarity value also decreases slightly near 2020 (Fig. 3). The pattern is highly robust with different model parameterizations (Methods and Extended Data Fig. 5). These observations suggest not only a pause but also a turning-back of the rotation by a small amount.

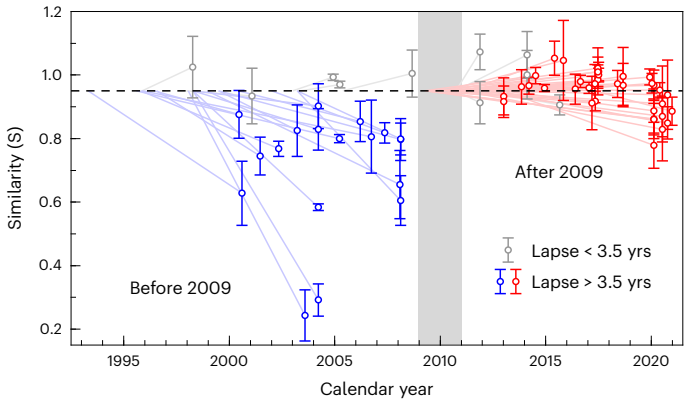

Fig. 3 | *S* of the inner-core waves from two subsets of doublets. In one subset (left), both events of a doublet are before 2009; in the other subset (right), both events are after 2009. Each line segment plots a doublet from the origin time of the earlier event and the reference *S* of 0.95 (the dashed horizontal line) to the origin time of the later event and the corresponding *S* horizontally and vertically, respectively. Each error bar represents an *S* measurement ± its measurement error (σ_s; see Methods). The shaded vertical bar indicates the 95% CI for the time of the turning point for the pattern change from the ddt data (see main text).

Observations of a multidecadal variation from 1964 to 2021

We also investigated the ddt measurements for a well-known path from the SSI region to the station COL in Alaska, which has doublet events in analogue records dated back to the 1960s[7,19]. We conducted a new systematic search and obtained 31 ddt measurements from doublets in 1964–2021 (Methods, Supplementary Information and Supplementary Table 5). The standard for doublet quality is higher than that in previous studies[19,33], though lower than that for the doublets above.

https://doi.org/10.1038/s41561-022-01112-z

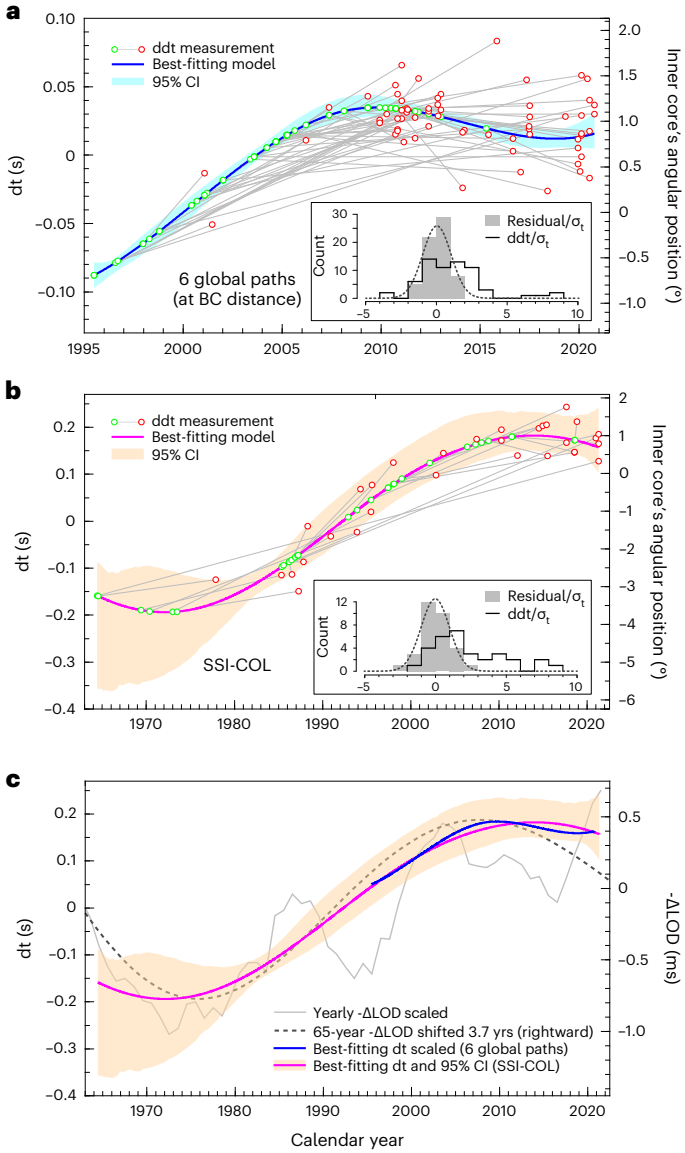

Fig. 4 | Global temporal change of DF's travel time (dt) and the comparison with the ΔLOD. Note that the dt is proportional to the amount of the inner-core rotation (or its angular position); here, the amount of rotation is estimated from our recent determination of the averaged rotation rate (0.127° per year) for the time period of 1991–2010[35], but the position of 0° is arbitrarily set at the year 2000. **a**, The best-fitting curve and 95% CI for the six global paths at BC distance and the region. Each segment denotes a scaled ddt measurement, plotted from the point on the curve at the origin time of the earlier event (green point) to a point offset by the scaled ddt (divided by the path-dependent factor; Extended Data Fig. 4) at the origin time of the later event. The inset shows the histograms (with an increment of 1.0) of the ddt measurements and residuals normalized by the corresponding measurement uncertainty (σ_t) and the dashed line shows a standard normal distribution with the same sample size as the indication of the uncertainty level (Methods). **b**, Same as **a** but for the path of the lower-quality SSI doublets to the COL station in Alaska. **c**, Comparisons between the trends of dt in **a** and **b** and the Earth's −ΔLOD. The 65-year component −ΔLOD (grey, dashed) is extracted from the yearly averages[40] (grey, solid) and shifted to the later time by 3.7 years for the optimal correlation.

We obtained the accumulated amount of the inner-core rotation from the ddt measurements with a similar method as above (Methods). The result from this path is consistent with the paused (or slightly overturned) rotation in the recent decade. During the same time span as above (mid 1995 to late 2020), the best-fitting curve of the path has nearly the same shape as that of the above global paths, as indicated by a nearly perfect correlation coefficient (at zero lag) of 0.97. The rotation from the late 1970s to the early 2000s is nearly steady, which is consistent with the previous result of ref. 19. However, the result also indicates another overturn or a slowdown of the rotation around the early 1970s. Although fewer observations are available, much smaller temporal changes for the early period (the 1960–1970s) are clearly observable in the original seismograms (Extended Data Fig. 6). The overall trend of the best-fitting spline behaves as a multidecadal oscillation with its period of about seven decades, although the result has relatively larger uncertainties than the global paths (Fig. 4b). A recent study[34] detects an overturn of the inner-core rotation around 1971 by two pairs of nuclear blasts, which in fact supports our observed change around the same time in a multidecadal oscillation.

Geodynamic implications of the multidecadal pattern

The simultaneous disappearance of the inner-core waveform temporal change along all paths in the recent decade (Figs. 2 and 3 and Extended Data Figs. 1–3) and the consistent pattern of the ddt measurements (Fig. 4 and Extended Data Fig. 4) strongly suggest a rigid body rotation of the inner core. The global and simultaneous pattern is much less compatible with the model of rapid localized growth or melting at the ICB[22–24]. The rotation is not purely steady, with a significant rate in the earlier decades[35] but a much smaller rate in the most recent decade and the 1960–1970s.

The inner core is believed to be dynamically linked with its outer layers, predominately through the EM coupling with the outer core[2] and gravitational coupling with the mantle[12]. The EM torque drives the inner-core rotation and is of the order of 10^{16}–10^{20} Nm (ref. 2–4,15). The gravitational torque slows down the rotation and meanwhile slightly deforms its shape for gravitational equilibrium with the maximum gravitational torque on the order of 10^{19} to 10^{21} Nm (ref. 12–14,16). Consequently, the kinetics of the inner core is controlled by the competition of the EM and gravitational torques[14,15]. Assuming that the inner core was rotating at the rate of 0.1° per year[27,35] before the 2000s and gradually stopped its rotation within a decade from the early 2000s to the early 2010s, the acceleration is estimated as 1.8×10^{-19} s^{-2}. With the inner-core moment of inertia of 5.86×10^{34} kg m^2 (ref. 4), the net torque on the inner core is around 1.1×10^{16} Nm. A small imbalance between the EM and gravitational torques is sufficient to change the inner-core rotation as observed here.

The slightly overturned rotation around 2009 and another overturn in the early 1970s, as well as relatively steady rotation in-between (Fig. 4b), suggest that the inner core is probably in an oscillation with a dominant period of about seven decades. Surprisingly, the multidecadal periodicity of the inner-core rotation coincides with several important geophysical observations, especially the length of day (LOD) variation (ΔLOD; Extended Data Fig. 7) and magnetic field changes, which both have a dominant periodicity of six to seven decades[36,37]. The common oscillation with six–seven-decade periodicity seems to indicate a resonance system across different Earth layers (Extended Data Fig. 8). The well-observed multidecadal oscillations in the ΔLOD and magnetic field have been largely explained by torsional oscillations of the outer core and the core–mantle coupling[36–39]. The newly revealed oscillating pattern of the inner-core rotation could be the result of the EM coupling with the outer core and gravitational coupling with the mantle[12,14,15].

The model of the mantle–inner-core gravitational coupling predicts a similar trend between the long-period −ΔLOD and the angular position of the inner core[13]. The six–seven-decade component of observed −ΔLOD[40] and the amount of the inner-core rotation during 1964–2021 resolved in this study has a high correlation coefficient of 0.92 at zero lag and an optimal value of 0.97 at a small lag of 3.7 years, which is highly consistent with the model prediction (Fig. 4c and Extended Data Fig. 7). The small lag may result from the time of viscous relaxation of the inner core under the gravitational coupling[13] or the

perturbation of the outer-core torsional flows in the tangent cylinder by EM coupling[41,42]. Nevertheless, an enigmatic lag of about two decades is well recognized between the highly correlated ΔLOD and magnetic signals, indicating the coupling system is complicated, not simply at the core–mantle boundary[37]. The complicated coupling and resonating system may indeed involve the inner core[39].

Interestingly, the same multidecadal periodicity is also well observed in the Earth's climate system[43,44], especially the global mean temperature and sea level rise. An ultimate explanation for the multidecadal climate oscillations is still being sought that includes extraterrestrial origins[45]. On the other hand, high correlations are also found recently, at zero lag, between global mean temperature and −ΔLOD[46] and between global mean sea level and magnetic dipole changes[40]. In addition, both vertical and horizontal displacements at the Earth surface can be excited by an oscillating inner core and torsional outer-core flows under gravitational coupling[47–49]. Consequently, the multidecadal periodicity of the climate system might also originate from the oscillating core–mantle system, through the surface deformations and the exchange of angular momentum from the core and mantle to the surface. As such, our finding may imply dynamic interactions between the deepest and shallowest layers of the solid Earth system (Extended Data Fig. 8).

Online content

Any methods, additional references, Nature Portfolio reporting summaries, source data, extended data, supplementary information, acknowledgements, peer review information; details of author contributions and competing interests; and statements of data and code availability are available at https://doi.org/10.1038/s41561-022-01112-z.

References

1. Buffett, B. A. Earth's core and the geodynamo. *Science* **288**, 2007–2012 (2000).
2. Gubbins, D. Rotation of the inner core. *J. Geophys. Res. Solid Earth* **86**, 11695–11699 (1981).
3. Glatzmaier, G. A. & Roberts, P. H. A three-dimensional convective dynamo solution with rotating and finitely conducting inner core and mantle. *Phys. Earth Planet. Inter.* **91**, 63–75 (1995).
4. Glatzmaier, G. A. & Roberts, P. H. Rotation and magnetism of Earth's inner core. *Science* **274**, 1887–1891 (1996).
5. Vidale, J. E. & Earle, P. S. Fine-scale heterogeneity in the Earth's inner core. *Nature* **404**, 273–275 (2000).
6. Creager, K. C. Inner core rotation rate from small-scale heterogeneity and time-varying travel times. *Science* **278**, 1284–1288 (1997).
7. Song, X. Joint inversion for inner core rotation, inner core anisotropy, and mantle heterogeneity. *J. Geophys. Res. Solid Earth* **105**, 7931–7943 (2000).
8. Attanayake, J., Thomas, C., Cormier, V. F., Miller, M. S. & Koper, K. D. Irregular transition layer beneath the earth's inner core boundary from observations of antipodal PKIKP and PKIIKP waves. *Geochem. Geophys. Geosyst.* **19**, 3607–3622 (2018).
9. Tanaka, S. & Hamaguchi, H. Degree one heterogeneity and hemispherical variation of anisotropy in the inner core from PKP(BC)–PKP(DF) times. *J. Geophys. Res. Solid Earth* **102**, 2925–2938 (1997).
10. Niu, F. & Wen, L. Hemispherical variations in seismic velocity at the top of the Earth's inner core. *Nature* **410**, 1081–1084 (2001).
11. Sun, X. & Song, X. Tomographic inversion for three-dimensional anisotropy of Earth's inner core. *Phys. Earth Planet. Inter.* **167**, 53–70 (2008).
12. Buffett, B. A. Gravitational oscillations in the length of day. *Geophys. Res. Lett.* **23**, 2279–2282 (1996).
13. Buffett, B. A. & Creager, K. C. A comparison of geodetic and seismic estimates of inner-core rotation. *Geophys. Res. Lett.* **26**, 1509–1512 (1999).
14. Buffett, B. A. & Glatzmaier, G. A. Gravitational braking of inner-core rotation in geodynamo simulations. *Geophys. Res. Lett.* **27**, 3125–3128 (2000).
15. Aurnou, J. & Olson, P. Control of inner core rotation by electromagnetic, gravitational and mechanical torques. *Phys. Earth Planet. Inter.* **117**, 111–121 (2000).
16. Davies, C. J., Stegman, D. R. & Dumberry, M. The strength of gravitational core–mantle coupling. *Geophys. Res. Lett.* **41**, 3786–3792 (2014).
17. Song, X. & Richards, P. G. Seismological evidence for differential rotation of the Earth's inner core. *Nature* **382**, 221–224 (1996).
18. Vidale, J. E., Dodge, D. A. & Earle, P. S. Slow differential rotation of the Earth's inner core indicated by temporal changes in scattering. *Nature* **405**, 445–448 (2000).
19. Zhang, J. et al. Inner core differential motion confirmed by earthquake waveform doublets. *Science* **309**, 1357–1360 (2005).
20. Yang, Y. & Song, X. Temporal changes of the inner core from globally distributed repeating earthquakes. *J. Geophys. Res. Solid Earth* **125**, e2019JB018652 (2020).
21. Poupinet, G., Ellsworth, W. L. & Frechet, J. Monitoring velocity variations in the crust using earthquake doublets: an application to the Calaveras Fault, California. *J. Geophys. Res. Solid Earth* **89**, 5719–5731 (1984).
22. Wen, L. Localized temporal change of the Earth's inner core boundary. *Science* **314**, 967–970 (2006).
23. Yao, J., Tian, D., Sun, L. & Wen, L. Temporal change of seismic Earth's inner core phases: inner core differential rotation or temporal change of inner core surface? *J. Geophys. Res. Solid Earth* **124**, 6720–6736 (2019).
24. Yao, J., Tian, D., Sun, L. & Wen, L. Comment on "Origin of temporal changes of inner-core seismic waves" by Yang and Song (2020). *Earth Planet. Sci. Lett.* **553**, 116640 (2021).
25. Yang, Y. & Song, X. Origin of temporal changes of inner-core seismic waves. *Earth Planet. Sci. Lett.* **541**, 116267 (2020).
26. Yang, Y. & Song, X. Reply to Yao et al.'s comment on "Origin of temporal changes of inner-core seismic waves". *Earth Planet. Sci. Lett.* **553**, 116639 (2021).
27. Wang, W. & Vidale, J. E. Earth's inner core rotation, 1971 to 1974, illuminated by inner-core scattered waves. *Earth Planet. Sci. Lett.* **577**, 117214 (2022).
28. Zhang, J., Richards, P. G. & Schaff, D. P. Wide-scale detection of earthquake waveform doublets and further evidence for inner core super-rotation. *Geophys. J. Int.* **174**, 993–1006 (2008).
29. Cao, A., Masson, Y. & Romanowicz, B. Short wavelength topography on the inner-core boundary. *Proc. Natl Acad. Sci. USA* **104**, 31–35 (2007).
30. Song, X. & Dai, W. Topography of Earth's inner core boundary from high-quality waveform doublets. *Geophys. J. Int.* **175**, 386–399 (2008).
31. Yao, J., Sun, L. & Wen, L. Two decades of temporal change of Earth's inner core boundary. *J. Geophys. Res. Solid Earth* **120**, 6263–6283 (2015).
32. Efron, B. & Tibshirani, R. J. *An Introduction to the Bootstrap* (Chapman and Hall/CRC, 1994).
33. Tkalčić, H., Young, M., Bodin, T., Ngo, S. & Sambridge, M. The shuffling rotation of the Earth's inner core revealed by earthquake doublets. *Nat. Geosci.* **6**, 497–502 (2013).
34. Wang, W. & Vidale, J. E. Seismological observation of Earth's oscillating inner core. *Sci. Adv.* **8**, eabm9916 (2022).
35. Yang, Y. & Song, X. Inner core rotation captured by earthquake doublets and twin stations. *Geophys. Res. Lett.* **49**, e2022GL098393 (2022).
36. Braginsky, S. I. Torsional magnetohydrodynamic vibrations in the Earth's core and variations in day length. *Geomagn. Aeron.* **10**, 1–8 (1970).

37. Roberts, P. H., Yu, Z. J. & Russell, C. T. On the 60-year signal from the core. *Geophys. Astrophys. Fluid Dyn.* **101**, 11–35 (2007).
38. Hide, R. Interaction between the Earth's liquid core and solid mantle. *Nature* **222**, 1055–1056 (1969).
39. Jault, D. in *Earth's Core and Lower Mantle* (eds Jones, C. A. et al.) 73–95 (CRC Press, 2003).
40. Ding, H., Jin, T., Li, J. & Jiang, W. The contribution of a newly unraveled 64 years common oscillation on the estimate of present-day global mean sea level rise. *J. Geophys. Res. Solid Earth* **126**, e2021JB022147 (2021).
41. Zatman, S. & Bloxham, J. Torsional oscillations and the magnetic field within the Earth's core. *Nature* **388**, 760–763 (1997).
42. Zatman, S. in *Earth's Core: Dynamics, Structure, Rotation* (eds Dehant, V. et al.) 233–240 (American Geophysical Union, 2003).
43. Schlesinger, M. E. & Ramankutty, N. An oscillation in the global climate system of period 65–70 years. *Nature* **367**, 723–726 (1994).
44. Gervais, F. Anthropogenic CO_2 warming challenged by 60-year cycle. *Earth-Sci. Rev.* **155**, 129–135 (2016).
45. Scafetta, N., Milani, F. & Bianchini, A. A 60-year cycle in the meteorite fall frequency suggests a possible interplanetary dust forcing of the Earth's climate driven by planetary oscillations. *Geophys. Res. Lett.* **47**, e2020GL089954 (2020).
46. Zotov, L., Bizouard, C. & Shum, C. K. A possible interrelation between Earth rotation and climatic variability at decadal time-scale. *Geod. Geodyn.* **7**, 216–222 (2016).
47. Ding, H. & Chao, B. F. A 6-year westward rotary motion in the Earth: detection and possible MICG coupling mechanism. *Earth Planet. Sci. Lett.* **495**, 50–55 (2018).
48. Dumberry, M. & Bloxham, J. Variations in the Earth's gravity field caused by torsional oscillations in the core. *Geophys. J. Int.* **159**, 417–434 (2004).
49. Greff-Lefftz, M., Pais, M. A. & Mouël, J.-L. L. Surface gravitational field and topography changes induced by the Earth's fluid core motions. *J. Geod.* **78**, 386–392 (2004).

Methods

Derivation of *S* in the presence of noise

A parameter (*S*) to measure the waveform similarity is used in this study (for example, in Fig. 2). Without the presence of noise, the *S* value is the same as the cross-correlation coefficient (CC) between the two waveforms. However, if the noise is present, the CC is affected by the noise level. Thus, we introduce the *S* parameter, which corrects for the influence of the noise, as a measure of the waveform similarity.

Assuming two time series (with the mean removed) $\mathbf{T_1}$ and $\mathbf{T_2}$ consist of Gaussian random noise $\mathbf{N_1}$ and $\mathbf{N_2}$ and highly similar waveform signals $\mathbf{W_1}$ and $\mathbf{W_2}$ ($|\mathbf{N_1}|$ and $|\mathbf{N_2}|$ are usually much smaller than $|\mathbf{W_1}|$ and $|\mathbf{W_2}|$), that is:

$$\mathbf{T_1} = \mathbf{W_1} + \mathbf{N_1}, \tag{1}$$

$$\mathbf{T_2} = \mathbf{W_2} + \mathbf{N_2}, \tag{2}$$

their CC can be computed as:

$$CC_{(T_1,T_2)} = \frac{T_1 \cdot T_2}{\sqrt{T_1 \cdot T_1} \times \sqrt{T_2 \cdot T_2}} \tag{3}$$

where the dot indicates dot product. Define the signal-to-noise ratios (SNRs) of the two time series as:

$$snr_1 = \frac{RMS(T_1)}{RMS(N_1)} = \sqrt{T_1 \cdot T_1 / N_1 \cdot N_1}, \tag{4}$$

$$snr_2 = \frac{RMS(T_2)}{RMS(N_2)} = \sqrt{T_2 \cdot T_2 / N_2 \cdot N_2}. \tag{5}$$

where RMS represents root mean square. Assuming the dot product between a random noise series and another series (excluding itself) is negligible, thus:

$$T_1 \cdot T_2 = W_1 \cdot W_2 + N_1 \cdot N_2 + N_1 \cdot W_2 + N_2 \cdot W_1 \approx W_1 \cdot W_2, \tag{6}$$

$$\begin{aligned} T_1 \cdot T_1 &= W_1 \cdot W_1 + N_1 \cdot N_1 + 2 \times N_1 \cdot W_1 \approx W_1 \cdot W_1 + N_1 \cdot N_1 \\ &= W_1 \cdot W_1 \times (1 + N_1 \cdot N_1 / W_1 \cdot W_1). \end{aligned} \tag{7}$$

From equations (4) and (7), we have:

$$T_1 \cdot T_1 \approx W_1 \cdot W_1 \times snr_1^2/(snr_1^2 - 1), \tag{8}$$

Similarly,

$$T_2 \cdot T_2 \approx W_2 \cdot W_2 \times snr_2^2/(snr_2^2 - 1). \tag{9}$$

Combining equations (3), (4), (8) and (9):

$$\begin{aligned} CC_{(T_1,T_2)} &\approx \frac{W_1 \cdot W_2}{\sqrt{W_1 \cdot W_1 \times snr_1^2/(snr_1^2-1)} \times \sqrt{W_2 \cdot W_2 \times snr_2^2/(snr_2^2-1)}} \\ &= \frac{CC_{(W_1,W_2)}}{\sqrt{snr_1^2/(snr_1^2-1)} \times \sqrt{snr_2^2/(snr_2^2-1)}}. \end{aligned} \tag{10}$$

S is defined as the CC of the corresponding noise-free signals, that is, $CC_{(W_1,W_2)}$ in equation (10):

$$S = CC_{(W_1,W_2)} \approx \sqrt{snr_1^2/(snr_1^2-1)} \times \sqrt{snr_2^2/(snr_2^2-1)} \times CC_{(T_1,T_2)}. \tag{11}$$

It is essentially the CC of the original noisy time series, $CC_{(T_1,T_2)}$, times a scaling factor ($f = \sqrt{snr_1^2/(snr_1^2-1)} \times \sqrt{snr_2^2/(snr_2^2-1)}$) from their SNRs to correct for the influence of the noises. If the SNRs of both traces are very large, $f \approx 1$ and the *S* value is the same as the $CC_{(T_1,T_2)}$.

Doublet datasets

We conducted new systematic searches for more doublets using available seismic data until early 2021, in the vicinity of the known doublets associated with the temporal changes of the inner core from previous studies[19,20,22,28–31]. The low magnitude threshold of the earthquakes is 4.5 from the Preliminary Determinations of Epicenters catalogue, which is generally lower than that in the previous studies to increase possible data. The doublets are searched out by assessing the waveform similarity of the available non-inner-core arrivals for every two events within 0.5° (based on the Preliminary Determinations of Epicenters catalogue), which is similar to our recent systematic global search[20]. More detailed descriptions of the seismic data, waveform preprocessing, doublet searching procedure and final datasets are presented in the Supplementary Information.

Measurements of *S* and estimation of uncertainty

As the core arrivals are quite different before and after the PKP caustic of around 145° (Fig. 1), we used different strategies for the two distance groups. For the BC group, the outer-core BC phase is a reliable reference for waveform alignment, as it is relatively energetic and shows indiscernible temporal changes[19,20]. We used a 5-s window from the onset of BC to align the waveforms by cross-correlation. For the window of DF (from its onset to the onset of BC), we computed the CC at zero lag and converted it to the *S* value based on the SNRs of their DF arrivals based on equation (11), where the SNR is defined as the RMS amplitude of the signal window divided by that of a 10-s preceding noise window as in equations (4) or (5). For the CD group, the inner-core arrivals (CD and DF phases) are relatively close and their waveforms overlap. Temporal changes can be identified as changes in waveforms. Thus, we simply computed the maximum CC using a 15-s window from the onset of DF and converted it to the *S* value based on the SNRs. The long window contains the energy of DF, CD and their coda arrivals, and its length is consistent with that used for non-inner-core arrivals in searching doublets (Supplementary Information). For both distance groups, the threshold of the SNR is 2.0 and we obtained a total of 172 *S* measurements (Supplementary Table 3 and Extended Data Fig. 3).

S is defined to correct for the influence of noises on CC based on the SNRs of two noisy waveforms, under the assumption of Gaussian random noise with zero mean (see above). For the real data, however, the noise level is not ideally constant or Gaussian, so that *S* also has uncertainty. It could be larger than 1.0, which is obviously an overestimation, if the noise level in the signal window is smaller than the preceding noise window.

We approximated the uncertainty (σ_s) for the *S* as a function of the corresponding SNRs from real data. Here, we used a large amount of waveform data from the 192 SSI doublets (Supplementary Table 1) for the statistical approximation. The non-SSI doublets are much fewer (Supplementary Table 2) and are hence not included. The *S* is essentially the CC times the scaling factor (*f*), which is related to the SNRs (equation (11)). As *f* increases (that is, smaller SNRs), the *S* measurements become more scattered (Supplementary Fig. 1a). In Supplementary Fig. 1a, we divided all the measurements into six bins based on the value of *f*. The σ_s could be approximated as the standard deviation (s.d.) of the *S* measurements in each bin, which shows a strong linear correlation with *f* (Supplementary Fig. 1b). The result of linear regression is $\sigma_s = 0.423 \times (f-1) + 0.009$. When the scaling factor is 1.0 (that is, noise-free), the σ_s is slightly positive (0.009), which may be due to small contributions from the tiny source difference to the uncertainty. In addition, the average *S* in each bin is between 0.97 and 1.00, except for the bin with the largest *f* (noisiest case; Supplementary Fig. 1a), whose average *S* is slightly below 0.95. As the onsets of the non-inner-core waves were picked with an automatic algorithm, short-term average over long-term average, near the predicted arrival time[20], the slightly lower average *S* might result from the inclusion of the noise segment in the CC window when the time picks are not accurate in the presence of the stronger noise.

Nevertheless, we used $S = 0.95$ as a reference to evaluate the temporal changes of the inner-core waves, above which we considered the waveform change insignificant. Also note that the minimum value of S is 0 because we rounded the negative CC values to 0. See Supplementary Table 3 for all the S measurements.

Measurements of ddt and estimation of uncertainty

We only focused on the temporal changes in the differential time for the paths in the BC group, because the energetic and consistent outer-core BC (and AB) arrivals provide a reliable reference for the waveform alignment[19,20]. The ddt measurement procedure (mainly the choice of the signal window) and its uncertainty estimation follow the same way as in our recent study[20]. When BC is aligned with cross-correlation using a 5-s window from its onset, we obtained the relative lag time of DF (ddt) corresponding to the maximum CC of the first 2-s DF arrivals. Here, we used a very short window of 2 s because we only focused on the relative shift of the first motion. In addition, the maximum CC could be very low in a full DF window with waveform changes in the coda (for example, Fig. 2b), making the lag-time measurement less reliable. In our recent study[20], we established an empirical equation to estimate the uncertainty (1 s.d.) of ddt (σ_t) from all possible factors, except the inner-core temporal changes, with a large amount of waveform data from equation in the study[20], that is:

$$\sigma_t = \sqrt{0.0151 \times (r_{df1}^2 + r_{df2}^2) + 0.0080 \times (r_{bc1}^2 + r_{bc2}^2) + (0.0133)^2}\ \text{s}, \quad (12)$$

where the r is the RMS of 10-s noise window preceding the DF onset divided by the peak energy in the signal window (2-s window for DF or 5-s window for BC), and the subscripts df1, df2, bc1 and bc2 denote the DF arrivals of the earlier and the later events, and their BC arrivals, respectively. Note that $1/r$ also represents a ratio of signal to noise (peak of signal over RMS of noise), but is different from the SNR defined above (RMS of signal over RMS of noise, equations (4) and (5)) for the S measurements. We discarded those with maximum CC of DF below 0.85 or $1/r$ of DF below 4.0 and obtained 64 ddt measurements from the high-quality global doublets (Paths 3–8) and 31 measurements from the lower-quality SSI doublets to station COL (Supplementary Tables 4 and 5). In addition, the 31 SSI doublets are searched out with a lower-quality threshold than the above doublets as well as those in our earlier study[20]; to compensate for their doublet quality and lower the weighting of the poorer-quality doublets in the inversion below, we slightly scaled-up their uncertainties (from equation (12)) by a factor inversely proportional to the corresponding doublet quality, which is indicated by the waveform similarity of their outer-core arrivals (see Supplementary Information for details).

Inversion of the inner-core rotation from the ddt measurements

We assumed that doublets in the same small patch to the same receiver sample the same lateral velocity gradient. However, the velocity gradients sampled by different patches may vary. Under the model of inner-core rotation, the lateral gradients are not large enough to produce observable travel time changes along most paths[20], which are not considered in this study. Therefore, besides the variable rotation rate, the temporal variation of DF's travel time also depends on the path, which is related to the magnitude of the lateral gradient along the path and the ray angle crossing the gradient.

We used a cubic spline to invert the change of DF's travel times (dt) as a function of the calendar time along different paths, $g(t) \times p_n$, where t is the calendar time, $g(t)$ is the spline function and p_n is a scaling factor associated with the path (the subscript n denotes the path number and ranges from 3 to 8). These scaling factors represent the relative lateral velocity gradients between different paths. A cubic spline is uniquely defined by the position and derivates of its starting and ending points, as well as the positions of all the knots in-between. Our final choice is a simple two-piece uniform (with equal intervals) spline after testing the goodness of fit with different splines (see below). The t starts at $T_0 = 1995.49$ (29 June 1995) and ends at $T_2 = 2020.77$ (9 October 2020) from the catalogue information of the earthquakes related to all the ddt measurements (Supplementary Table 4). The midpoint, T_1, is 2008.13 (17 February 2008). The baseline of the spline could be arbitrary because the ddt measurements only provide constraints on the shape of the spline. We simply set the starting point at 0, that is, $g(T_0) = 0$, and removed the mean value of the spline later (Fig. 4). Thus, there are four free parameters controlling the spline, $g'(T_0)$, $g'(T_2)$, $g(T_1)$ and $g(T_2)$, where $g'(T_0)$ and $g'(T_2)$ are the time derivatives at the two endpoints. In addition, there are six paths with the ddt measurements and hence six factors related to the paths (p_3 to p_8). We used Path 5 (PCT-KZ) as the reference by setting p_5 to 1.0, which has more ddt measurements than the other paths, to avoid the trade-offs between $g(t)$ and p_n. The other five factors (p_3, p_4, p_6, p_7 and p_8) are free parameters in the inversion. The predicted ddt (ddt_{pred}) along Path n is $p_n \times (g(t_2) - g(t_1))$, where t_1 and t_2 are the decimal year of the earlier and later events, respectively. The four parameters controlling the spline and the five parameters related to the paths are searched out with the neighbourhood algorithm[50]. The parameter search is performed by minimizing a misfit function (M), which is defined as $M = \sum\left((\text{ddt}_{\text{obs}} - \text{ddt}_{\text{pred}})^2/\sigma_t^2\right)$, and the number of the observed ddt measurements (ddt_{obs}) is 64 and σ_t is an uncertainty of the corresponding ddt_{obs}. In this way, the ddt measurements with larger uncertainty have smaller weightings in the inversion. The best-fitting spline and the path-dependent factors of the optimal model are shown in Fig. 4 and Extended Data Fig. 4.

We used the standard bootstrap method[32] to evaluate the model uncertainty. First, we constructed a new dataset by selecting 64 ddt measurements randomly (allowing repetition) from the original dataset (a total of 64 measurements). Second, we carried out the same joint inversion as above to obtain the spline coefficients and the path-dependent factors. Third, we repeated the above two steps 1,000 times and obtained 1,000 sets of optimal solutions. The 95% CI for the dt at any given time (Fig. 4) or the slope of dt in a certain period can be obtained from the 1,000 solutions of the bootstrap. From the bootstrapping, we also obtained the time of the change of the slope in $2009.8\pm^{1.2}_{0.8}$, and the slopes before and after 2009 at $9.12\pm^{0.72}_{0.52}$ ms yr^{-1} and $-1.58\pm^{1.21}_{1.11}$ ms yr^{-1}, respectively.

We explored more complex splines with more knots and evaluated the models from the statistics of the model residuals and data uncertainty (the posterior probability). The spline coefficients and the path-dependent factors are inverted in the same way by minimizing M with the neighbourhood algorithm[50]. If a model is ideally correct and fully removes the contribution of the inner-core rotation, the ddt residual is solely from its uncertainty. Normalized residuals of an ideal model, $(\text{ddt}_{\text{obs}} - \text{ddt}_{\text{pred}})/\sigma_t$, should follow the standard normal distribution $N(0,1)$ and the minimizer M thus follows a chi-squared distribution with υ degrees of freedom (64 measurements subtracted by the number of model constraints, 55 for the above two-piece spline model), that is, $M \approx \chi^2_\upsilon$, and is a classic indicator of the posterior model probability (for example, ref. 51). The expected value of M is υ and a model with M greater than the 95th percentile of the distribution can be rejected at 95% confidence level.

A simple two-piece uniform spline is sufficient to account for the ddt measurements along all the paths, leaving small residuals explainable by the measurement uncertainties (with M of 30.4 smaller than its expected value; also see the histogram in Fig. 4a). The complex models have negligible improvements in the model fitting and are within the uncertainty ranges of the simple spline (Extended Data Fig. 5a). Consequently, the simple spline represents well the pattern of our observations and we thus adopt the simple model to avoid overfitting.

We also tested another type of model with two linear segments to examine the change of the temporal slopes. The turning point of the slope change at $[b, \text{dt}(b)]$ was allowed to vary, which connects the start

of the first segment at $[T_1, 0]$ and the end of the second segment at $[T_2, \mathrm{dt}(T_2)]$. We inverted the values of b, $\mathrm{dt}(b)$, $\mathrm{dt}(T_2)$ and the path-dependent factors, and obtained the model uncertainty with the bootstrap method, in the same way as above. The best-fitting result and the uncertainty range are highly consistent with the simple spline model (Extended Data Fig. 5b). The second segment also shows a robust negative slope. From the bootstrapping, the 95% CI for the slopes of the two segments and the time of the turning point are $11.06\pm^{1.15}_{1.39}$ and $-2.16\pm^{0.60}_{0.98}$ ms yr^{-1} and $2007.38\pm^{0.83}_{1.46}$, respectively. The linear-segment model is for testing purposes only, as such a sudden change of slope is not physical. Nevertheless, the results are quite similar to those of the spline model above with small differences in the slopes and the turning point, which result purely from the parameter assumptions.

The temporal change of the SSI–COL path was inverted independently, which has a much longer duration from 1964 to 2021 (Fig. 4b). The path has 31 ddt measurements of relatively lower quality (Supplementary Information and Supplementary Table 5). We first corrected the ddt measurements for the small raypath difference from the potential mislocation of the lower-quality doublet events and/or the relocation of the station site in 1996 (by 4.3 km), using the relative time of the two outer-core AB and BC arrivals ($\tau_{AB} - \tau_{BC}$) and a coefficient of 0.4 (ref. 19), that is, subtracting 0.4 times the $\tau_{AB} - \tau_{BC}$ from the measured ddt. Then we inverted the temporal change of the corrected DF's travel times using the same method as above, except that here we used a five-piece uniform spline for a similar temporal resolution (decadal scale) to above. The fit to the data is reasonably good, as suggested by the normalized residuals (see the histogram in Fig. 4b). The 95% CI of the model (Fig. 4b) was also obtained from bootstrapping.

Data availability

The digital waveform data in this study are openly available from the Incorporated Research Institutions for Seismology Data Management Center (http://iris.edu) and Canadian National Seismograph Network (http://earthquakescanada.nrcan.gc.ca/stndon/CNSN-RNSC/index-en.php). The analogue waveforms from the station COL were collected and manually digitized by ref. 7, and those of the SSI doublets are available at https://doi.org/10.6084/m9.figshare.21548679.v1. The yearly averaged LOD measurements and the daily Earth Orientation Parameters series (EOPC04) are freely downloaded from the International Earth Rotation and Reference Systems (https://www.iers.org/IERS/EN/Home/home_node.html).

Code availability

The codes used in this study are available upon request.

References

50. Sambridge, M. Geophysical inversion with a neighbourhood algorithm—I. Searching a parameter space. *Geophys. J. Int.* **138**, 479–494 (1999).
51. Stephenson, J., Tkalčić, H. & Sambridge, M. Evidence for the innermost inner core: robust parameter search for radially varying anisotropy using the neighborhood algorithm. *J. Geophys. Res. Solid Earth* **126**, e2020JB020545 (2021).

Acknowledgements

We acknowledge the support from the National Key R&D Program of China (grant no. 2022YFF0800601 to X.S.), the National Natural Science Foundation of China (grant no. U1939204 to X.S. and grant no. 42104096 to Y.Y.) and China Postdoctoral Science Foundation (grant no. 2021M690203 to Y.Y.). The discussions with H. Ding and J. Chen helped improve our manuscript.

Author contributions

X.S. and Y.Y. conceived the study; Y.Y. processed the seismic data; Y.Y. and X.S. analysed the data and wrote the manuscript together.

Competing interests

The authors declare no competing interests.

Additional information

Extended data is available for this paper at https://doi.org/10.1038/s41561-022-01112-z.

Supplementary information The online version contains supplementary material available at https://doi.org/10.1038/s41561-022-01112-z.

Correspondence and requests for materials should be addressed to Xiaodong Song.

Peer review information *Nature Geoscience* thanks Severine Rosat, Susini De Silva, Thanh-Son Phạm and Januka Attanayake for their contribution to the peer review of this work. Primary Handling Editor: Louise Hawkins, in collaboration with the *Nature Geoscience* team.

https://doi.org/10.1038/s41561-022-01112-z

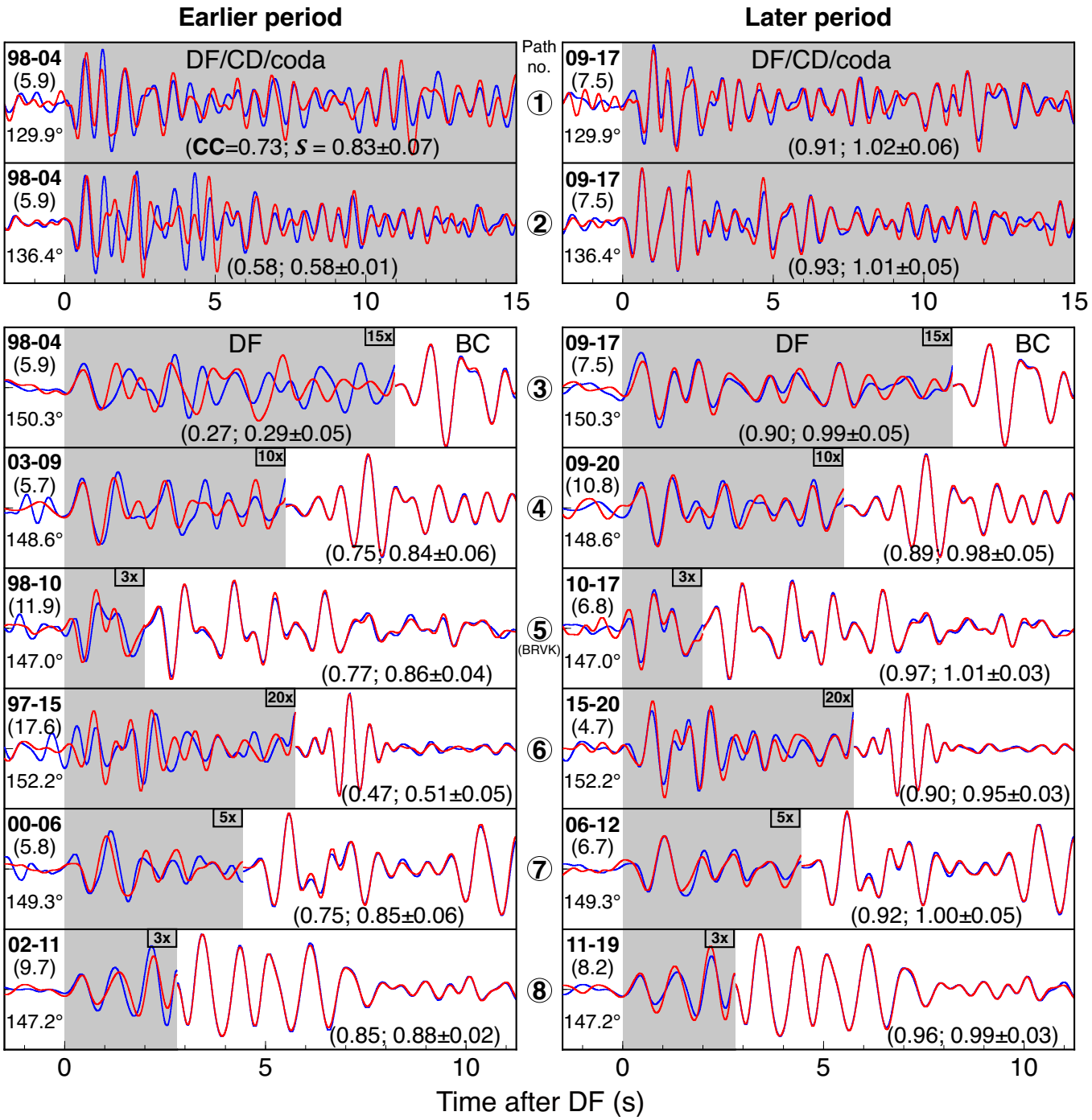

Extended Data Fig. 1 | Waveform comparisons of the multiplets of all the eight paths. Each row with two panels side by side shows the waveforms from the same multiplet, with the path number labeled in between. The left panels show pairs from the relatively old time period with the earlier event in the 1990s or early 2000s, while the right panels show pairs from the relatively recent time period with both events in the late 2000s or even later. The waveform plots and notations follow the same style as in Fig. 2.

https://doi.org/10.1038/s41561-022-01112-z

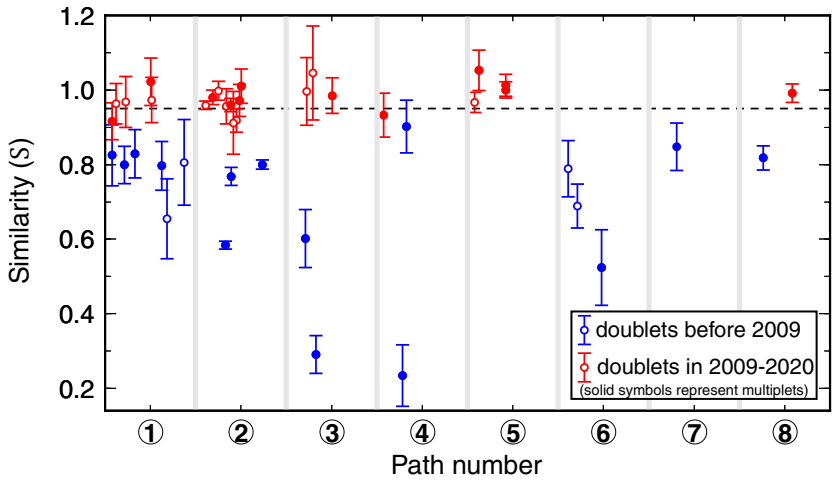

Extended Data Fig. 2 | Comparison of global similarity (*S*) measurements between two time periods. The *S* measurements and their corresponding uncertainty ranges (circles and vertical bars of $\pm\sigma_s$) of the inner-core waves along all the eight different paths are plotted but only from doublets with lapse over 3.5 years and the most recent data (year 2020 and after) are not included. In each path-bin, the horizontal position of each measurement represents the lapse of the doublet, which is normalized by an interval of 3.0 to 12.0 years. If a doublet belongs to a multiplet, we use solid circles to distinguish.

https://doi.org/10.1038/s41561-022-01112-z

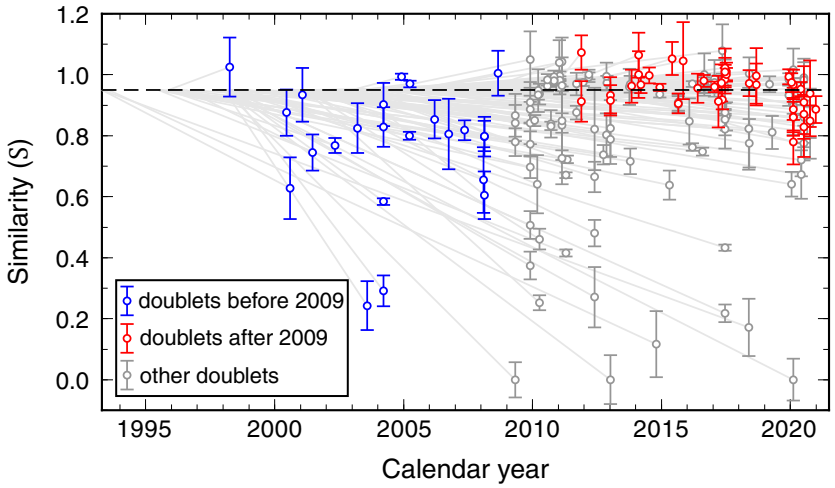

Extended Data Fig. 3 | All the *S* measurements of the inner-core waves in this study. The light gray line segments and error bars ($\pm\sigma_s$) are plotted in the same way as in Fig. 3. The measurements from the doublets with both events before 2009 (blue) or after 2009 (red) are also shown in Fig. 3. The other doublets (gray) have one event before 2009 and the other event after 2009.

https://doi.org/10.1038/s41561-022-01112-z

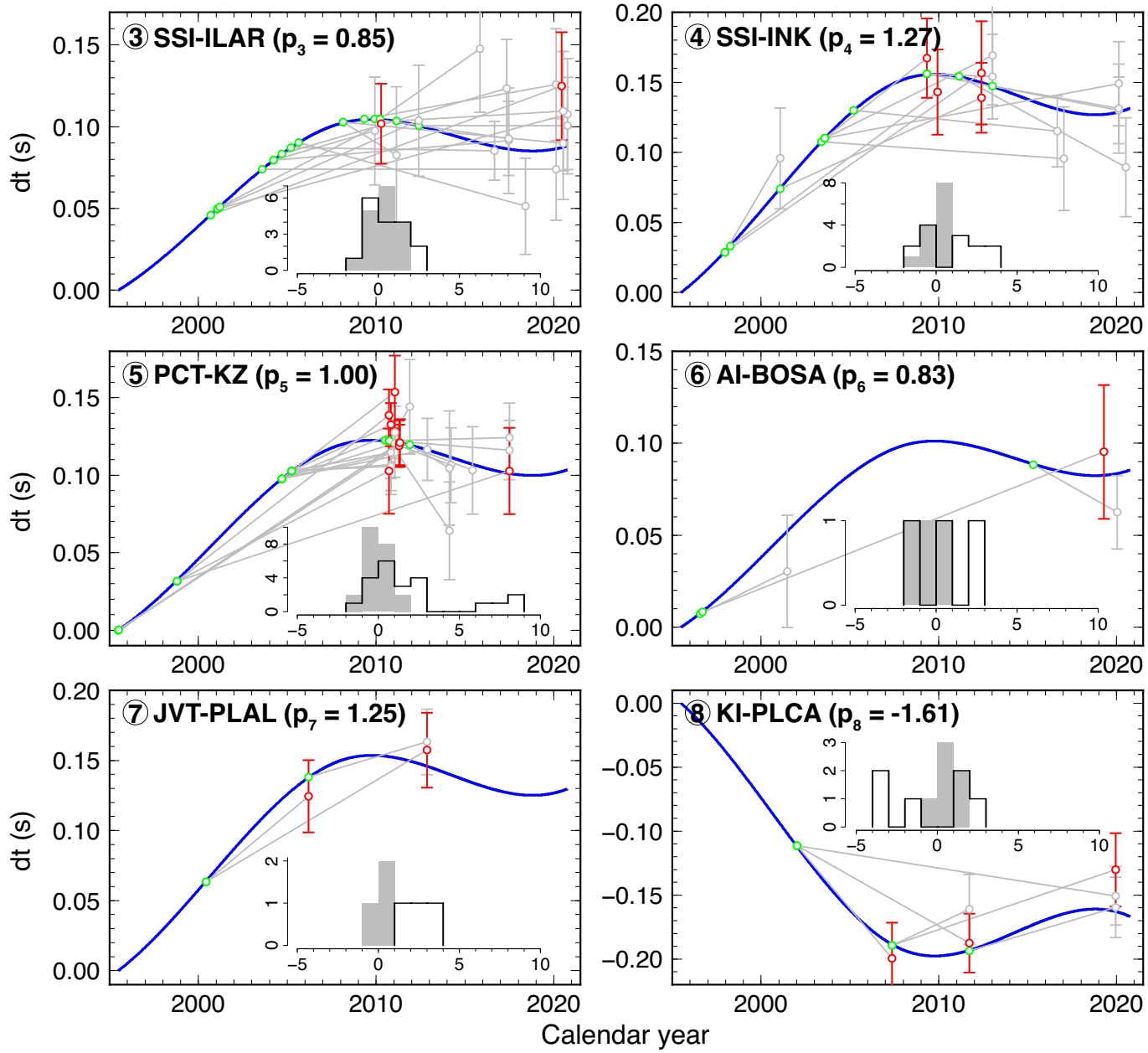

Extended Data Fig. 4 | Temporal changes of DF's travel time along the 6 paths at the BC distance range. In each panel, the best-fitting curve (solid blue line) is the path-dependent factor (p_n) multiplied by the same cubic spline from the joint inversion (Methods). The dt segment of each doublet is plotted in the same way as in Fig. 4. The uncertainty of each measurement ($\pm\sigma_t$) is plotted at the end of the segment, and large ddt measurements over $2\sigma_t$ are marked in red (others in gray). The histograms represent the distributions of the normalized ddt measurements and residuals, similar to those in Fig. 4.

https://doi.org/10.1038/s41561-022-01112-z

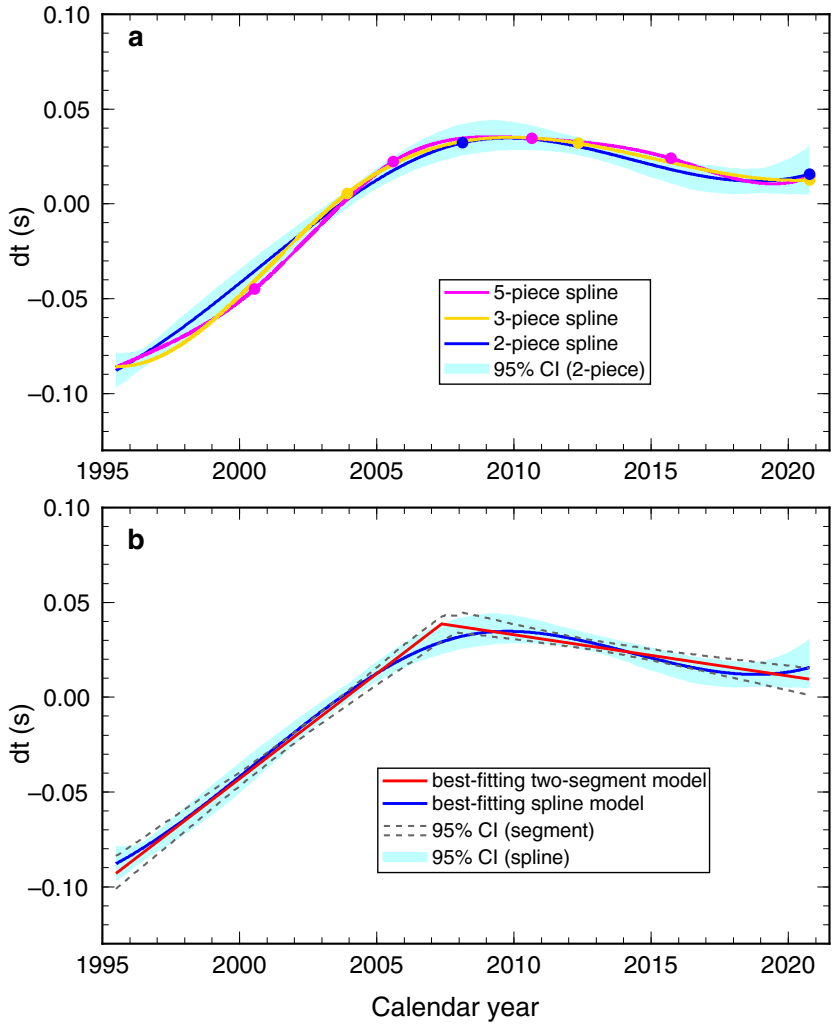

Extended Data Fig. 5 | Comparison of the best-fitting two-piece uniform spline with other models. (a) Other uniform splines with more knots. Here, we show the best-fitting 3-piece and 5-piece uniform splines. The circles with corresponding colors are the knots of the splines searched out in the inversion (Methods). (b) A model with two connected linear segments and its uncertainty from bootstrapping. Note that the mean values of the models in (a) and (b) have been removed.

https://doi.org/10.1038/s41561-022-01112-z

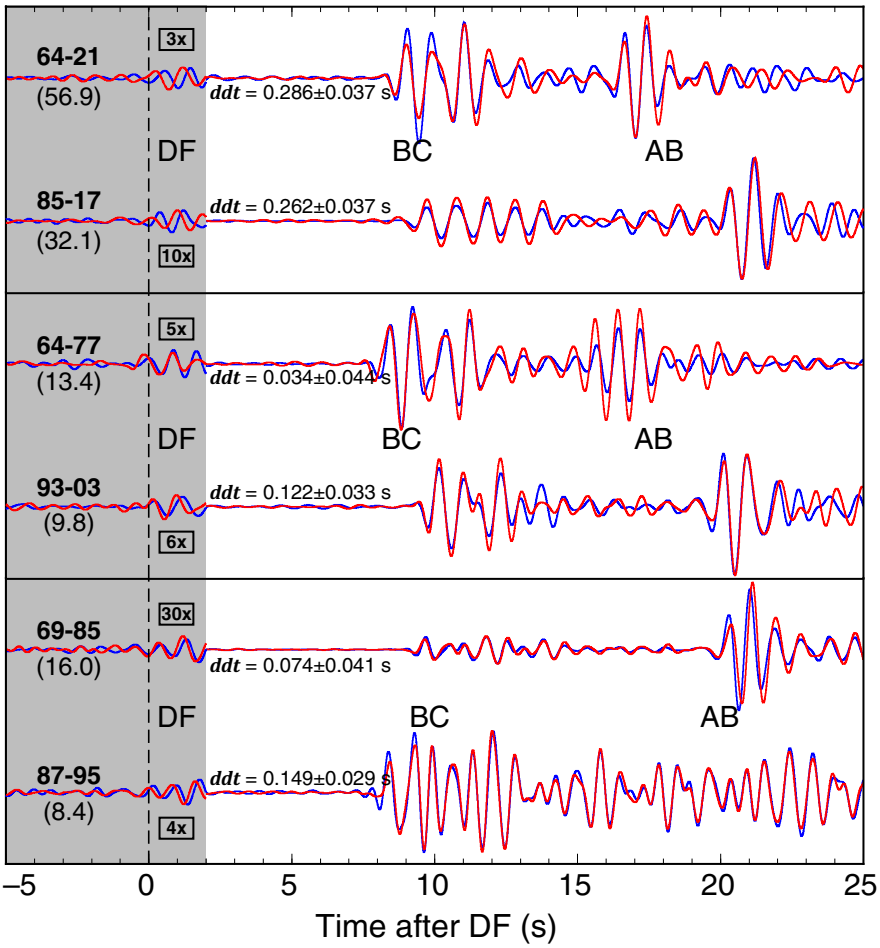

Extended Data Fig. 6 | Comparison of the ddt measurements between the early lower-quality SSI doublets sampling the 1960s and the later doublets. In each panel, the doublet on top covers the time period of the 1960s and early 1970s and has a much larger lapse (labeled in the paratheses) but smaller or comparable ddt than that of the bottom doublet. Note that the labeled ddt measurements have been corrected for the small difference in the epicentral distance of the two doublet events, as indicated by the relative time shift between the outer-core BC and AB arrivals (Methods). The waveform plots and the notations follow the same style as in Fig. 2c.

https://doi.org/10.1038/s41561-022-01112-z

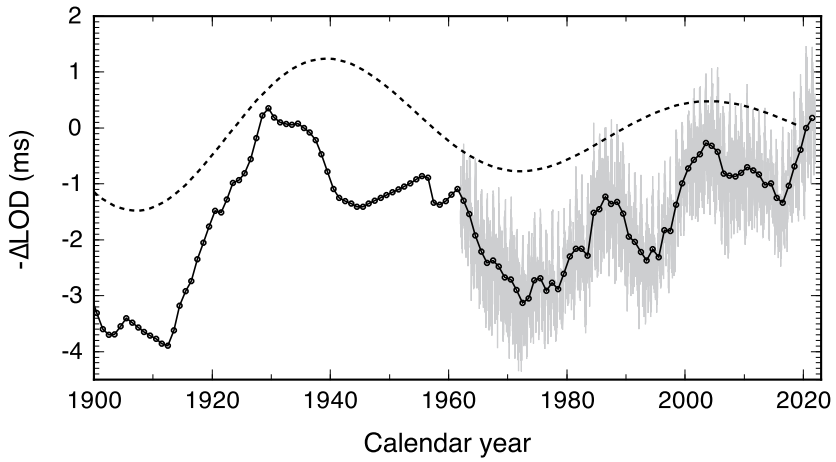

Extended Data Fig. 7 | Reverse of the length of day variations (-△LOD). The gray line shows the daily EOPC04 series, which is available in the time span of 1962 to the present day from the International Earth Rotation and Reference Systems (IERS). The yearly averaged -△LOD measurements (the circles connected by a solid black line) before 2008 are directly obtained from the IERS, and those after 2008 are computed from the daily EOPC04 series. The dotted line is the 65-year component of the -△LOD extracted by Ding et al.[40] using wavelet decomposition.

https://doi.org/10.1038/s41561-022-01112-z

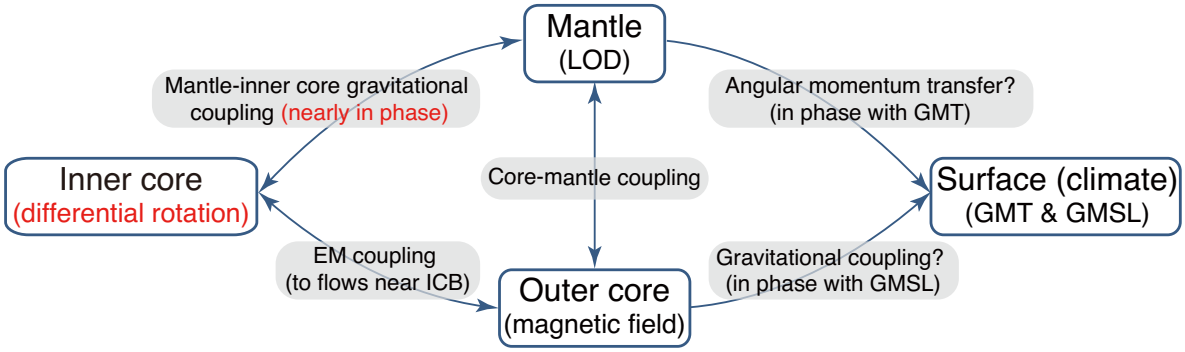

Extended Data Fig. 8 | A possible resonance Earth system with a period of 6–7 decades across different layers from the inner core to surface. The question marks indicate uncertain physical mechanisms yet. New observations of this study are highlighted in red.